IMAGING OF OSTEOLYTIC BREAST CANCER METASTASES WITH COMPUTED TOMOGRAPHY,

POSITRON EMISSION TOMOGRAPHY AND SINGLE PHOTON

EMISSION COMPUTED TOMOGRAPHY

By

Lindsay Craig Johnson

Thesis

Submitted to the Faculty of the

Graduate School of Vanderbilt University

in partial fulfillment of the requirements

for the degree of

MASTER OF SCIENCE

in

Biomedical Engineering

May, 2010

Nashville, Tennessee

Approved:

Professor Todd E. Peterson

Professor Mark D. Does

ACKNOWLEDGEMENTS

TABLE OF CONTENTS

LIST OF TABLES

LIST OF FIGURES

Figure   Page

LIST OF ABBREVIATIONS AND NOMENCLATURE

Abbreviation	Full Name
1. ^{18}F	Fluoride-18
2. ^{99m}Tc	Technetium-99m
3. BLI	Bioluminescence Imaging
4. BS	Bone Scintigraphy
5. BV	Bone Volume
6. CL	Control Limb
7. CT	Computed Tomography
8. H&E	Hematoxylin and Eosin
9. HU	Hounsfield Units
10. LL	Lesion Limb
11. MDP	Methylene Diphosphonate
12. MRI	Magnetic Resonance Imaging
13. OSEM	Ordered Subset Expectation Maximization
14. PET	Positron Emission Tomography
15. ROI	Region of Interest
16. SNR	Signal to Noise Ratio
17. SPECT	Single Photon Emission Computed Tomography
18. TV	Total Volume

CHAPTER I

INTRODUCTION

Motivation

The most common site that breast cancer metastasizes to is bone. Patients who have

metastatic cancer develop bone lesions in 30% to 85% of cases, with 50% of those having bone

as the first metastatic site (Hamaoka, Madewell et al. 2004). Determining the presence of breast

cancer metastases is standard clinical practice with at-risk patients. This is done with a variety of

imaging modalities such as Bone Scintigraphy (BS), Magnetic Resonance Imaging (MRI), Planar

Radiography, Computed Tomography (CT), Positron Emission Tomography (PET), and/or Single

Photon Emission Computed Tomography (SPECT) (Even-Sapir 2005). The goal of clinical imaging

is to identify the presence of metastases and use that information to help determine a

treatment regimen or to assess treatment response. In small-animal imaging, the same

modalities are typically used but research studies are more focused on determining quantifiable

changes in bone volume or bone metabolism to better gauge underlying biological processes.

Several studies performed preliminary investigations into how well some of these modalities

perform in small animals (Cowey, Szafran et al. 2007; Hsu, Virk et al. 2008), but these

investigations have either not been done longitudinally, not considered the effects of radiation

dose on the subject, or had inconclusive results. This project will investigate quantitative and

qualitative imaging of MDA-MB-231 osteolytic bone metastases in small animals using CT,

SPECT, and PET.

Biological Background

In healthy bone there is generally a balance between osteoclastic and osteoblastic activity which, respectively build and resorb bone matrix. This balance is maintained by a variety of growth factors that can be found both around bone milieu and within the bone matrix itself (Datta, Ng et al. 2008). Bone matrix backbone is composed of type 1 collagen and hydroxyapatite ($Ca_5(PO_4)_3OH$) and typically has various growth factors incorporated into it (Teitelbaum 2000). Although many cancer types (e.g. breast and prostate) have high rates of metastases that form in bone (Society 2008), this project focuses on osteolytic breast cancer metastases. For a typical osteolytic cancer line, tumor cells that have migrated to bone release osteolytic factors which then induce osteoclastic activity to increase bone resorption. Bone resorption then leads to additional secretion of growth factors from bone that further stimulate the tumor cells, resulting in a vicious cycle (Figure 1) of tumor growth (Guise, Kozlow et al. 2005).
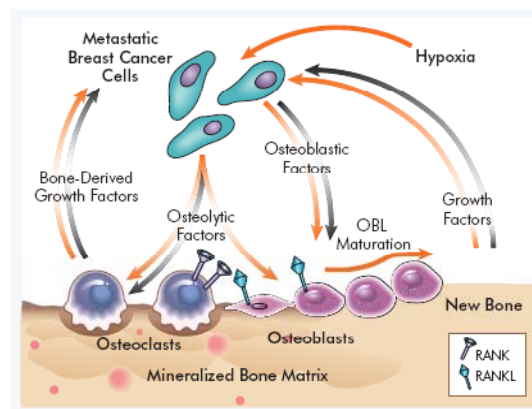
Figure 1: Metastatic cancer cells hijack naturally occurring osteoclasts and osteoblasts by releasing osteolytic factors, which recruit osteoclasts to degrade bone. Bone degradation then releases bone-derived growth factors that fuel more factors to be released by the metastatic cells (Guise, Mohammad et al. 2006).

This process leads to an increase in osteoblastic activity as an attempt to keep up with the heightened osteoclastic activity, causing an overall increase in bone growth and resorption. In osteolytic lesions this increase is unbalanced with increased osteoclastic activity causing overall bone loss (Datta, Ng et al. 2008).

Bone Imaging with Computed Tomography

Morphological data can help to visualize changes in volume in both metastatic osteolytic and osteoblastic lesions. Small-animal studies are typically done with x-ray radiography as the method is quick, inexpensive, and usually has a lower radiation dose than CT. Because radiography is a 2-D technique, it typically only shows whether a lesion is present and its approximate size from visual inspection. Reconstructed CT images result in 3-D images that allow viewing of individual slices for better localization of changes and for the potential quantification of the size of bone lesions.

Previous studies have used microCT to investigate bone volume changes in the tibia of a female rat that underwent an ovariectomy. One ovariectomized and one control rat were imaged with microCT at three time points. Images were registered using a mutual information-based algorithm and then differences were quantified using a simple threshold method. The ovariectomized rat was determined to have lost 25% of epiphyseal trabecular and 60% of metaphyseal trabecular bone volume at 4 weeks. In this study reproducibility error was determined to be less than 3% in bone volume measurements (Waarsing, Day et al. 2004). Although this method was applied to rats in a non-cancer model, it demonstrates the quantitative capabilities of measuring bone loss with microCT.

Imaging with CT at multiple time points over the course of a study can give valuable information about disease progression in bone without having to sacrifice the animal for

histomorphometry. In longitudinal studies, fewer animals are needed to gain statistical significance and disease progression can be followed in the same animal over time. However, there is a concern that the ionizing nature of CT can cause a high enough radiation dose to the subject in repeated scans that the dose will have a therapeutic effect on the cancer model being studied. An absorbed radiation dose as small as 1cGy reduced tumor volume in a mouse model of lymphoma relative to controls (Bhattacharjee and Ito 2001). Because effects of radiation are highly dependent on the cell line being studied it is necessary to perform preliminary studies ensuring that longitudinal CT scans do not affect tumor growth. Although this project focuses on using MDA-MB-231 osteolytic cell line, one study has been done to determine effects of multiple CT scans using the human breast cancer cell line MDA-MB-435. This study did not attempt to quantify the bone loss with CT due to poor visualization in the CT images. CT scans were acquired weekly for five weeks with an approximate absorbed radiation dose of 1Gy per scan. Bioluminescence imaging (BLI) was used to quantify lesion size and it showed that there was no significant difference between CT-exposed and non-CT exposed tumor sizes in mice ($p>0.05$). However, histomorphometry of the CT-exposed group was shown to have a statistically significant increase ($p=0.029$) in tumor area relative to the non-CT exposed group (Cowey, Szafran et al. 2007). These potential effects require careful consideration when determining imaging protocols.

<center>Functional Bone Imaging</center>

Introduction

Although morphological imaging is useful, imaging of bone matrix turnover could potentially allow for earlier detection of metastases and treatment response. In small-animal

applications this could lead to a better understanding of the underlying biological processes of bone metastases formation. Although there are a variety of modalities capable of functional bone imaging, two main nuclear medicine techniques are investigated herein: PET and SPECT. Both modalities have similar tracers that can be used to image bone turnover.

Positron Emission Tomography

The PET tracer commonly used for imaging of bone turnover is ^{18}F-Fluoride (^{18}F). Imaging with ^{18}F requires having a cyclotron close by due to its 110 minute half life. When injected, ^{18}F is directly incorporated into the bone matrix by replacing a hydroxyl group on the hydroxyapatite, resulting in fluoroapatite. Due to the turnover continually occurring on portions of healthy bone, ^{18}F preferentially deposits on bones located axially over appendicularly as well as at bone joints over middle portions of long bone (Bridges, Wiley et al. 2007).

Several studies have investigated how sensitive ^{18}F PET is in detecting and quantifying bone metastases compared to other imaging modalities in a clinical setting (Schirrmeister, Guhlmann et al. 1999; Even-Sapir, Metser et al. 2006; Chen, Huang et al. 2007; Schirrmeister 2007). Similar studies are less common in small-animal applications, but some initial investigations have been performed. One representative study investigated osteolytic, osteoblastic and mixed lesions in a prostate cancer mouse model (Hsu, Virk et al. 2008). In this study ^{18}F-FDG and ^{18}F-Fluoride in conjunction with high resolution microCT images were compared. ^{18}F-FDG is commonly used to image tumors as it has an increased uptake in areas of high cellular glucose metabolism (Gambhir 2002). Osteolytic, osteoblastic and mixed prostate cancer cell lines were injected into the tibia of mice and tumor growth over time was quantified. For each prostate cancer cell line, lesion size and signal intensity were determined for ^{18}F and ^{18}F-FDG through hand-drawn regions of interest (ROIs) around the lesion area and compared to

5

the non-injected contra-lateral limb. Quantification from MicroCT images was used as an outcome measure in osteolytic lines, while histomorphometric analysis was used in the mixed and osteoblastic lines. Pure osteoblastic lesions quantified with ^{18}F were determined to have significantly larger lesions at each time point (P>0.05) as well as higher signal intensity (P<0.05), which can be seen in Figure 2. Also with this cell line, osteoblastic lesions were not detectable on radiographs until the 6th week after injection, while they were detectable in ^{18}F PET/CT images as early as 4 weeks.
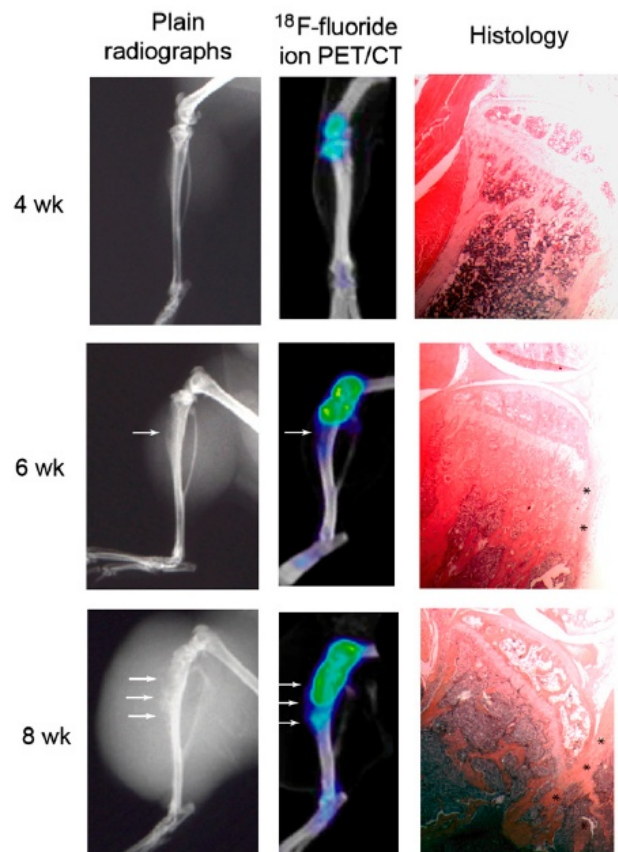
Figure 2: Radiography, ^{18}F PET/CT and histology show initial uptake at week 4, followed by increased update in subsequent weeks as osteoblastic lesion begins building new bone (Hsu, Virk et al. 2008).

Mixed lesions were only evaluated with ^{18}F-FDG and osteolytic lesion changes measured on the ^{18}F PET images were not found to be significant (Hsu, Virk et al. 2008). This study shows the

potential that functional bone imaging with ^{18}F PET/CT has, but this method has yet to be quantified or attempted in a breast-cancer metastatic model.

Single Photon Emission Computed Tomography

As with PET, SPECT can be utilized to image bone turnover by using technetium-99m methylene diphosphonate (^{99m}Tc-MDP). ^{99m}Tc-MDP is known to be incorporated into the crystalline structure of hydroxyapatite as well as chemically adsorbed onto the surface of hydroxyapatite (Kanishi 1993). It has also been shown that accumulation of MDP into the bone does not correlate to the number of osteoblasts present; it is associated with the mineral process of bone matrix building (Toegel, Hoffmann et al. 2006). This association with matrix building and subsequent osteoblastic activity is a desired characteristic because the presence of osteoblasts does not directly relate to the amount of bone turnover.

Although using planar bone scintigraphy with ^{99m}Tc-MDP is the first step in determining the presence of bone metastases in clinical situations (Hamaoka, Madewell et al. 2004), this method is not ideal in the case of small-animal imaging as simple detection of metastases is generally not the primary study objective. One small animal study utilized BLI and microSPECT imaging of mice that had a cardiac injection of MDA-MB-435 breast cancer cell line. BLI was performed weekly, while ^{99m}Tc-MDP SPECT was only done at the 5 week endpoint of the study. For microSPECT imaging, mice were injected with 3mCi of ^{99m}Tc-MDP and given a 3 hour uptake time before imaging with X-SPECT (Gamma Medica Inc: Northridge, CA). Results of these images and the corresponding histology can be seen in Figure 3. It was determined that this SPECT imaging protocol was not sensitive enough to detect significant changes between hind limbs with lesions and hind limbs without lesions (P=0.086) (Cowey, Szafran et al. 2007). Currently

there are no reported results with ^{99m}Tc-MDP SPECT on either mixed or pure osteoblastic cell

lines, or its use in longitudinal studies.
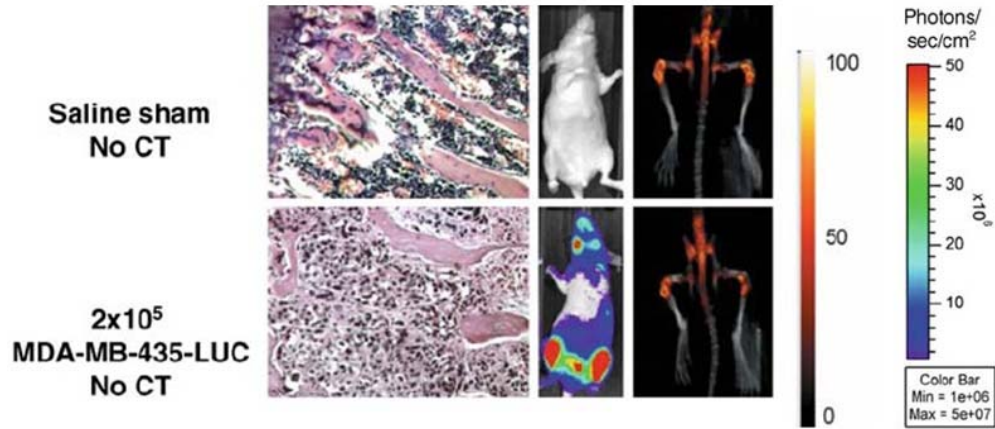
Figure 3: Histology, BLI, and SPECT overlaid on CT images of a control and lesion mouse at study end point. BLI shows significant uptake in tumor regions, while SPECT changes are not distinguishable (Cowey, Szafran et al. 2007).

CHAPTER II

CT QUANTIFICATION OF TUMOR-INDUCED BONE LOSS

Introduction

Although X-ray radiography is the most common method for detecting the presence of bone lesions in preclinical studies, CT is often used when quantification of lesion size is necessary. As previously discussed, studies nvestigated using CT to measure bone volumes, but this was mainly done in rats. The goal of this study was to determine a repeatable method for estimating bone volume changes over time in mice with osteolytic bone lesions. This study used a tibia-injected MDA-MB-231 cell line, although the methodology is broadly applicable. To do this, a study of the effect of the radiation dose from CT scans on this specific cell line was performed. Next, a four-week longitudinal study of treated and untreated tumor-bearing mice was performed. Finally, analysis methods were developed to quantify tibia bone in order to investigate changes in bone volume over time.

Methods

Preliminary Radiation Effect Study

In order to investigate the reliability of using longitudinal CT scans as a quantitative measure of bone loss, preliminary studies must be performed to determine the effect of weekly irradiation on the mouse model. Two different CT protocols were performed using the Imtek MicroCat II, one high resolution (Bin-2), and one lower resolution (Bin-4), with imaging being performed 1, 2, or 3 time(s) over the four week study, and with one control group that did not receive any CT imaging. The Bin-2 protocol used 80 kVp, 500 μA with 900 msec per projection

and 600 projections over 360° for a total scan time of approximately 20 minutes, while the Bin-4

protocol was acquired with 80kVp, 500μA with 600msec per projection and 300 projections over

360° for a total scan time of approximately 10 minutes. All images were reconstructed to 512 ×

512 × 512 voxels, with Bin-2 having 0.08 × 0.08 × 0.062 mm^3 voxel size and Bin-4 having 0.159 ×

0.159 × 0.062 mm^3 voxel size. The radiation dose from Bin 2 and Bin 4 were estimated to be

148.3 mGy and 49.4 mGy respectively. These values were determined using work from Natasha

Monina, which was adapted from (Boone, Velazquez et al. 2004). Both protocols were

reconstructed with the same conebeam filtered back projection algorithm with a Hamming

filter. A secondary objective of this data set was to investigate how the different protocols affect

visualization of the bone lesions. The final protocol used was determined by the visual quality

and preliminary quantification of bone volume.

Two-Group Longitudinal Study

MDA-MB-231 tibia-injected mice were imaged using the Imtek MicroCAT II weekly for

four weeks. Sixteen mice were divided into two groups, one treatment group (n=8) and one

control group (n=8). All mice were injected in one tibia with tumor cells at week 0, and the

treatment group received one tail-vein injection of 5mg/kg of Zoledronic Acid on day 6 after

injection. Zoledronic Acid is known to slow bone degradation at the site of an osteolytic tumor

(Polascik 2009). Images were acquired at weeks 1, 2, 3, and 4 post injection for all 16 mice, using

the same Bin-2 protocol as was performed in the preliminary study, and were reconstructed to

have 512 × 512 × 512 voxels at a resolution of 0.15 × 0.15 × 0.212 mm^3 with a filtered back

projection and Hamming filter algorithm. Although not presented here, collaborators imaged

the same mice using a variety of other modalities including weekly GFP using Maestro, faxitron,

and end point Scanco microCT of extracted tibias and histomorphometry. These data were not

collected by the author and therefore are not included here, but data on all imaging modalities will be included in a peer-reviewed publication that will demonstrate correlation between microCT quantification procedures and other measures.

Quantification Procedure

Image quantification of bone volume was done using a threshold method based on Hounsfield Units (HU). Due to unstable detector performance and differences between intensity scales in each image, all images being quantified were first converted to Hounsfield Units (HU) to give them all the same intensity scale and allow for reasonable week to week comparisons. The HU scale defines standard intensity values for air and water as -1000 and 0 respectively. As is standard protocol, the plastic bed is assumed to have the same intensity of water. A range of values is generally given for the definition of HU for bone, but 1700 was chosen as it best created a linear fit with this data set. Hand-drawn ROIs of air, bed, and healthy bone in the same z-slices as the tibia were made and the average ROI value of each air, bed, and bone ROI was then applied to a linear fit of -1000, 0, and 1700, respectively. This linear fit was then used to convert all voxel values to HU. This process was performed at all 4 time points with each mouse. All image analysis was done using Amira 5.2 (Visage Imaging, Inc). Figure 4 and Figure 5 show a representative set of ROIs used to determine mean values and the subsequent linear transformation plot.
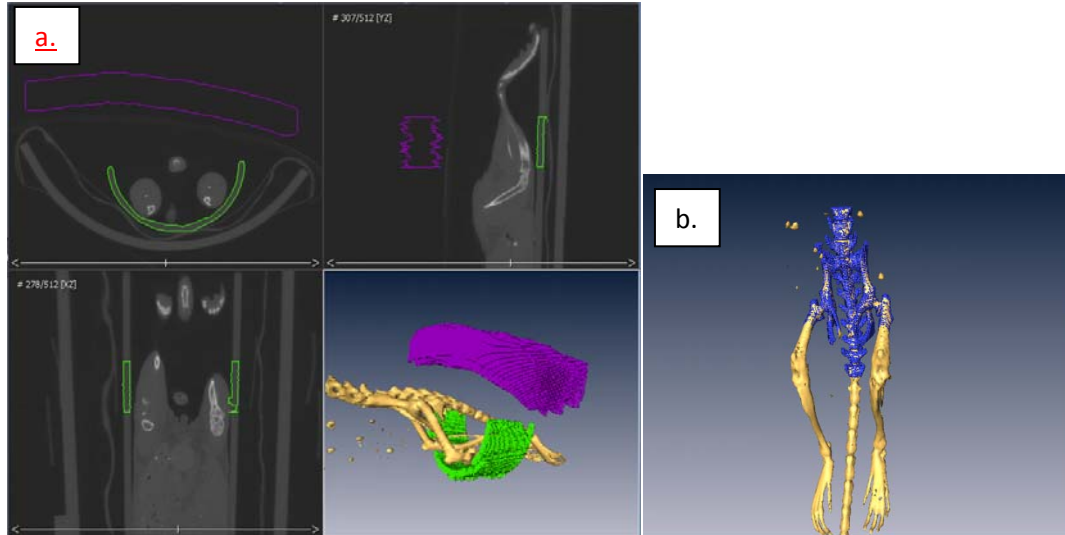
Figure 4: Panel a shows transverse, sagittal, and coronal views of air (purple) and bed (green) ROIs along with a 3-d rendering. Panel b shows the ROI used to determine mean bone intensity overlaying a bone isosurface of the image.
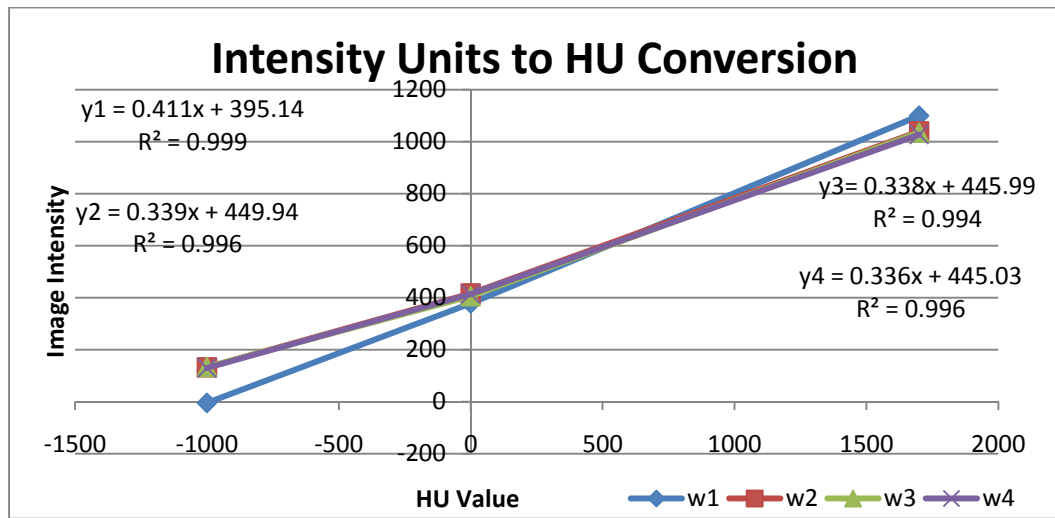
Figure 5: Graph shows one mouse's weekly scans with the three average ROI values plotted against their assigned HU value. Linear trend-lines were fitted to each data set and the resulting equation was used to transform each image voxel into HU.

Following conversion to HU, each image was roughly cropped into two parts: the tibia-region of the lesion limb (LL), and the contra-lateral tibia region for use as a control limb (CL). The LL images for all four time points were then registered to one another using Amira's Affine Registration function using the Correlation metric with a Quasi Newton optimizer step. The

same process was used on the 4 CL images. Each limb was then carefully cropped to extend from just below the patella but above the growth plate to the point where the tibia and fibula join, with the fibula being removed as well. This process is illustrated in Figure 6 and Figure 7.
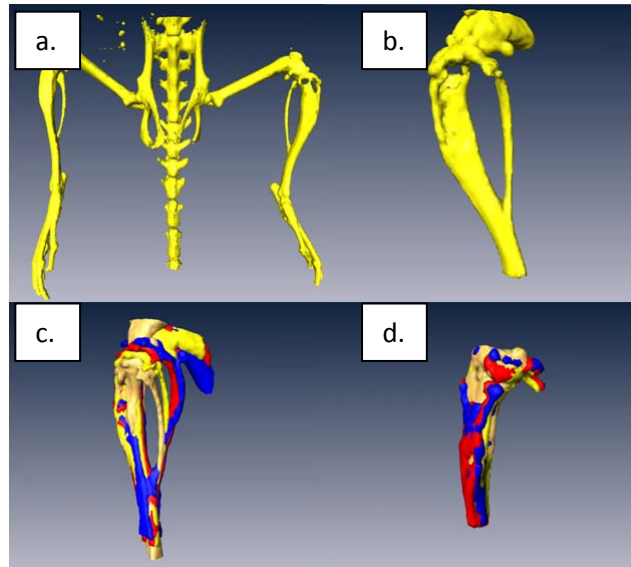
Figure 6: Representative isosurface views of one mouse's (a) original image, (b) roughly cropped image, (c) registration of all 4 images and (d) final cropped and registered images. Tan, yellow, red, and blue isosurfaces represent weeks 1, 2, 3, and 4 respectively. The registration shows how the fibula is moved as the tumor region becomes larger and pushes it further away from the tibia.
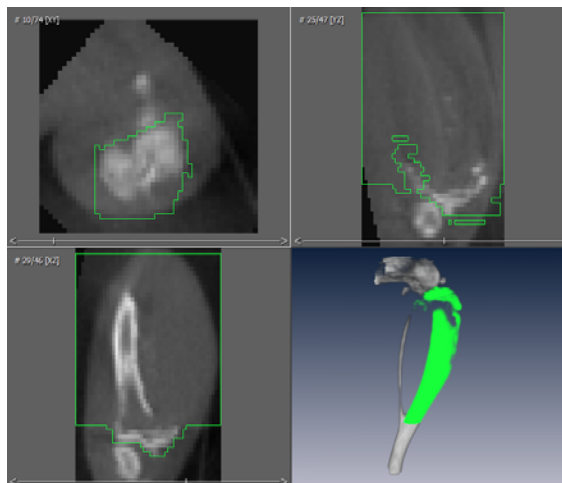
Figure 7: Representative x, y, and z slices of a typical final cropped image. Final volume rendering of the cropped region is in green, while the original roughly cropped region is in grey.

To determine the intensity threshold for delineating bone and non-bone voxels, varying HU thresholds were applied to the final cropped images and volumes were calculated for each HU threshold. One mouse's CL volume changes over four weeks can be seen in Figure 8, which shows that as the HU threshold becomes smaller, the percent change between weekly volumes becomes smaller. An ideal threshold will be high enough to minimize changes in CL data, but still be low enough to be sensitive to changes occurring in the LL. A threshold of 1000 HU was chosen because higher thresholds had a lower effect on the percent change between weeks. This choice is essentially the lowest HU value that minimized difference between weeks. This 1000 HU cutoff was then applied to the cropped section of bone to define what voxels are counted in the final bone volume. The number of voxels that were above the threshold were then summed and converted to a volume measure of the tibia.
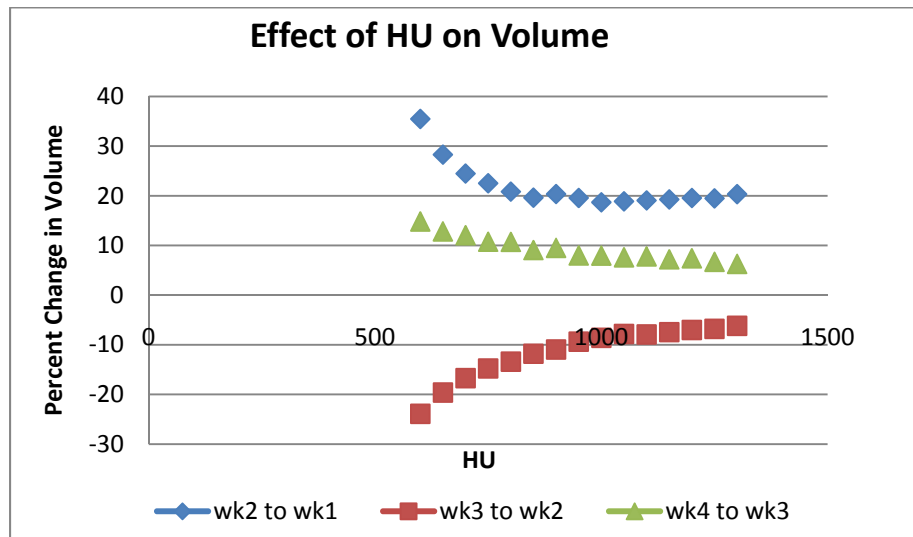
Figure 8: Percent changes in volume between subsequent weeks. Variation between weeks stabilizes at the 1000 HU cutoff.

Preliminary Radiation Effect Study

Groups of three mice were given either 3 Bin-2 CTs, 3 Bin-4 CTs, 2 Bin-2 CTs, 2 Bin-4 CTs, or 1 Bin-2 CTs, with one scan acquired per week. One group was only imaged immediately before sacrifice (no-CT group). After sacrifice, the region of bone and tumor below the growth plate was analyzed by histology. Hematoxylin and eosin (H&E) staining was performed on the slides and analyzed with Metamorph software. Bone region, tumor region and total area were identified on each slice and volumes were calculated. The percent of bone volume/total volume (% BV/TV), and percent tumor volume were then determined. Figure 9 shows the results of histology for the various groups. It was determined that differences between groups were not statistically significant. This initial investigation proves that it is possible to longitudinally image mice at a high resolution setting without causing the tumor size to decrease. Initial calculations of bone volume were attempted on two mice, one with Bin-2 and one with Bin-4 protocols. It was determined that although visual inspection of images did not greatly vary, reliable quantification was only possible with the Bin-2 protocol. Because of this fact, and that Bin-2 did not affect tumor size, the longitudinal study was performed with a Bin-2 protocol.
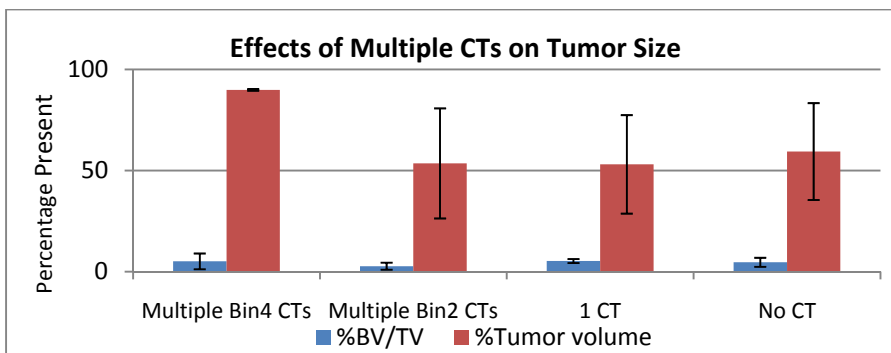
Figure 9: The percent of bone volume over total volume and percent of tumor volume is graphed with the standard error. Even multiple Bin-2 imaging does not lower tumor volume.

15

Two-Group Longitudinal Study

For each mouse, both CL and LL were quantified for each of the four time points. Results for the untreated group are shown in Figure 10 and Figure 11 and the treated control group in Figure 12 and Figure 13.
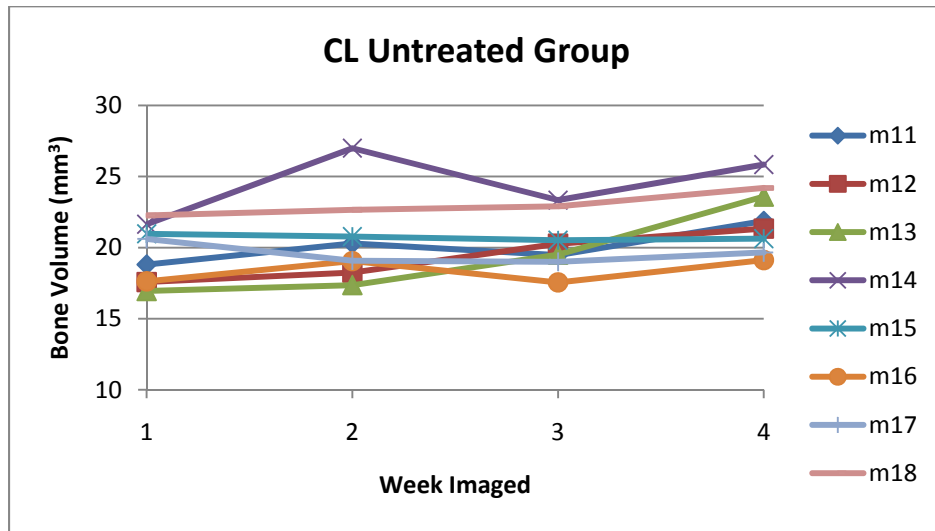
Figure 10: The CL in the untreated group is expected to have the same volume over the course of the study. This figure demonstrates the individual mice's volume trends which remain mostly stable.
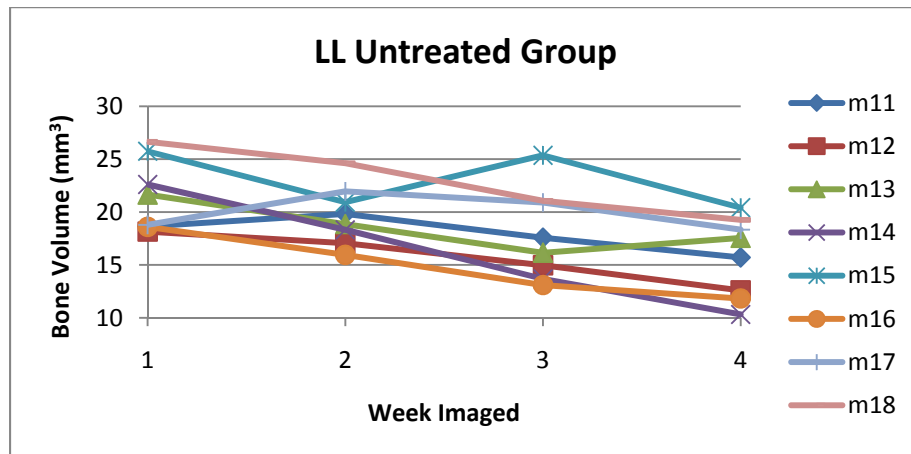
Figure 11: The LL of the untreated group is expected to have a decrease in volume as the tumor size increases and degrades the bone. This trend can be seen in individual mice.
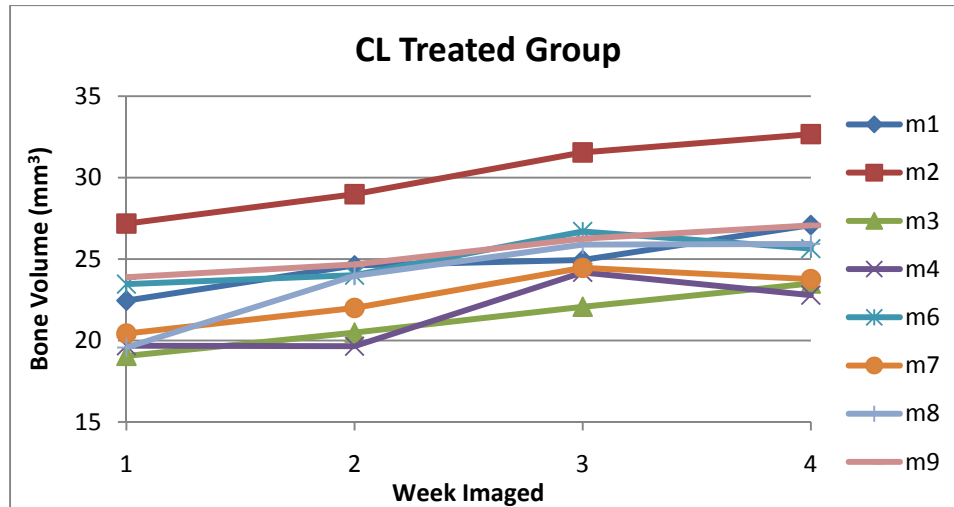
Figure 12: The CL of the treated group is expected not to significantly change over the period of the study. There appears to be a slightly increasing volume trend over time.
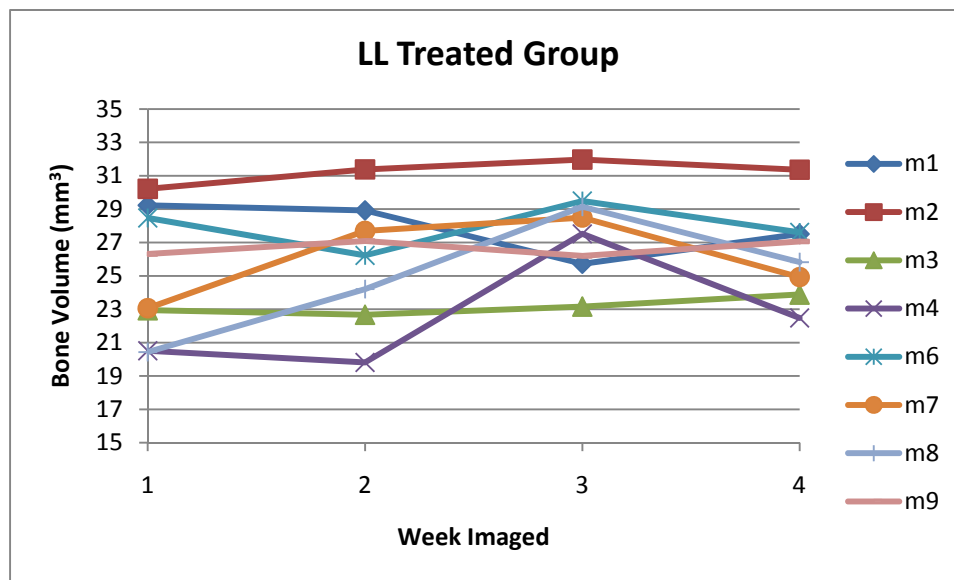
Figure 13: The LL of the treated group was expected to have a larger volume than that of the untreated LL. It can be seen that the treatment worked well enough to essentially eliminate bone loss due to the tumor.

Visual inspection of the quantification method shows reasonable bone volumes with only a few outliers that appear to have unreasonable volumes. Inter-animal variation can be seen in Figure 10 – 13, while intra-animal variation is more challenging to estimate as a variety

of factors could lead to differences in determined volumes. These factors include determination

of HU due to differing ROIs chosen, differences in cropping of images, and varying quality of the

CT imagines themselves. Statistical analysis was performed with the help of Lei Xu (Vanderbilt

University Department of Biostatistics). We fitted a linear mixed model to the data and included

random subject effect to account for the correlation of the longitudinal measurements from the

same subject. We used different slope parameters to capture the overall trend of the CT volume

measurements over time for each group. We first tested the hypothesis of whether the slope of

each group equaled zero. We then compared the slope between groups. To adjust for multiple

comparisons we used 0.05/8=0.006 as the cut off point for p-values being statistically significant.

Table 1 shows the results of the statistical analysis that compares the slopes to zero, while Table

2 shows the between group comparisons.

Table 1: The average slope of each group, in conjunction with its T-value and p-value are shown.

Group:	Slope	T-value	p-value
Untreated CL	0.4463	2.00	0.0483
Treated CL	1.2183	5.46	<0.0001
Untreated LL	-1.7637	-7.90	<0.0001
Treated LL	0.5953	2.67	0.009

Table 2: Slope trends compared for each group to determine statistical significance

Comparison	T-value	p-value
Differences between treated LL and untreated LL	-7.72	<0.0001
Differences between treated CL and untreated CL	2.53	0.0132
Differences between treated LL and treated CL	2.04	0.0443
Differences between untreated LL and untreated CL	3.67	<0.0001

From the results we can see that the CT volume measures decrease over time for the LL

area of the untreated group, and increase for other groups. The slopes are significantly different

from zero for the untreated LL group and for the treated CL area. Each week the CT volume measurement increased by a factor of 1.22 for the control area in the treated group, while it decreased by a factor of 1.76 for the lesion area in the treated group. The slope of changes are significantly different between the treated and untreated lesion volumes ($p<0.0001$) and are also significantly different between the lesion and the control volume in the untreated group ($p<0.001$).

In addition to testing for significance between groups, the time point at which the LL becomes significantly different from the CL in the untreated group is also of interest. The differences between lesion and control area for the untreated group at each time point were tested to determine the earliest time point at which the differences became significant. We fit a linear mixed model using the differences as the response variable and included random subject effect to account for the correlation of measurements over time. We included time as a factor. As we are making 4 comparisons we adjusted the threshold of p-value at $0.05/4=0.0125$. As can be seen from Table 3, the differences are statistically significant starting at week 3.

Table 3: Week 3 and week 4 show significant differences between CL and LL volumes in the untreated group.

	Mean Differences between LL and CL	p-value
Week 1	-1.796	0.2101
Week 2	2.668	0.0492
Week 3	4.269	0.0031
Week 4	8.080	<0.0001

Discussion

Preliminary Radiation Effect Study

It is important to understand the effects that radiation dose has on the model being studied. The preliminary study proved that frequent high-resolution microCT scanning does not affect tumor growth. Each cancer cell line has varying sensitivity to radiation dose, and can cause either rapid cancer growth or halt tumor growth all together. Because of the small effect frequent microCT scanning was found to have on this tumor cell line, the volume measures completed in the subsequent longitudinal study are assumed to not be influenced by the imaging being performed.

Two-Group Longitudinal Study

Although the treatment used is commonly applied in clinical applications, it has yet to be tested in the current MDA-MD-231 osteolytic cell line. This investigation proves that treatment significantly lowers bone loss due to the metastatic bone lesion. In addition, ability to quantify changes in bone volume changes in mice using microCT was validated. Although there were cases of outliers which can be seen in the graphs of Figure 10- 13 graphs, they did not affect the overall statistical significance of the analysis. Several attempts were made to determine the source of variation in the volume measurements that appeared to be outliers. For example, in the untreated control group, the LL on mouse 15 increases in volume between week 2 and 3, and then drops below the week 2's value at week 4. Visual inspection of images suggested that there was no apparent change in image quality between different time points.

To better gauge the source of variation, images from each week were converted to values of 0 or 1 for non-bone and bone regions as defined by the 1000 HU threshold. Week 3 was then subtracted by week 2 in order to visualize where the majority of changes were

20

localized. For mouse 15's set of subtracted binary images, this merely showed an overall increase in bone both along the outside edges of the bone and along the inside marrow region. This can be seen in Figure 14. One possible explanation for this could be due to the poor image quality of the microCT due to degraded detector performance during this study.
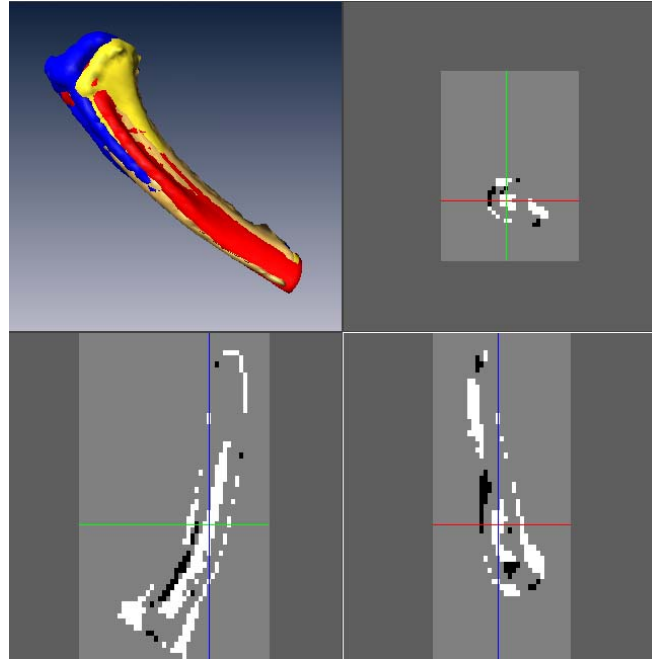
Figure 14: Tan, yellow, red, and blue isosurfaces represent weeks 1, 2, 3, and 4 of the same mouse. The three views of the subtraction image show the difference between the third and second week, with white voxels being present in week 3 but not week 2 and black voxels in week 2 but not week 3. Some changes are due to non-perfect registration, but the majority of the white voxels are due to an overall increase in the volume at week 3.

Also, this study proved that under the described imaging protocol it is possible to distinguish the presence of an osteolytic lesion based on quantitative assessment of changes in bone volume at three weeks after injection. In general, visual inspection of the images show lesions as early as one week after injection. Although CT provides reliable quantitative measures of volume changes, the protocol used does not allow for early detection. Ideally changes in bone caused by metastatic activity could be detected within the first week or two after cell injection.

This would allow for earlier quantification of treatment studies that would better resemble clinical procedures.

Results could potentially vary depending on the quality of the microCT system being used. Better, more reliable scanners could have the potential to produce a better signal to noise ratio (SNR) at smaller resolutions and therefore enable detection of volume differences at earlier time points. One main limitation of this study is the quality of the scanner used. At the time of imaging one portion of the detector was not functioning at an optimum level, and could have caused some degradation of image quality. Also, alternative imaging protocols could lead to better image quality. Although two different imaging protocols were investigated in the preliminary work, there could be other alternative protocols to better visualize small changes in bone. Because earlier detection is desirable, an additional investigation of functional bone imaging will be pursued in order to determine its ability to detect or quantify changes in osteolytic metastases.

CHAPTER III

RADIATION DOSE BASED COMPARISON OF PET AND SPECT FOR BONE IMAGING IN A MOUSE
MODEL OF OSTEOLYTIC METASTASES

Introduction

PET and SPECT Comparison

Due to the similarities of PET and SPECT imaging and given their individual strengths and

weakness, it is often difficult to determine which modality is best suited for a specific small-

animal imaging task. Although PET generally has better sensitivity, SPECT can have better

resolution in addition to being less expensive and having tracers with longer half-lives. Standard

measures of system characteristics such as spatial resolution, temporal resolution, or sensitivity

give some insight into the strengths of a specific imaging system but they do not fully

characterize how well a system will perform a specific task. This study will use imaging of

osteolytic bone lesions as the basis of comparison of PET and SPECT. Although there are many

overlapping imaging tasks between PET and SPECT, bone imaging will be used as a starting point

due to the availability of the ^{18}F and ^{99m}Tc MDP tracers. Even though the mechanism of

incorporation into bone is similar for these tracers, it has been shown that ^{18}F is incorporated

into bone at twice the rate of ^{99m}Tc MDP (Even-Sapir 2005). The varying strengths and

weaknesses of PET and SPECT in conjunction with the individual tracer properties leads to a

debate as to which modality will produce images of higher quality.

Motivation for Radiation Dose Based Study

As discussed previously, there are many advantages to longitudinal studies that image multiple times over the course of the study. But frequent imaging leads to an increased radiation dose to the animal. This radiation dose is of particular concern in studies that involve the progression of tumors, as the radiation dose received from imaging can act as a treatment and alter tumor growth and progression (Beir 1990; Bhattacharjee and Ito 2001). Because of this, the comparison study's imaging protocol will be based on injected activities of each tracer that deliver the same estimated radiation dose to the bone of the animal. Radiation dose values for ^{18}F can be estimated from previous work (Taschereau and Chatziioannou 2007), but corresponding data were not available for ^{99m}Tc-MDP at the start of this study.

Determination of "Fair" Comparison

Although starting with the same absorbed radiation dose to the mouse for each tracer is a practical starting point for a comparison study, absorbed dose alone does not ensure a "fair" comparison between modalities. Other considerations such as scan time, field of view, and reconstruction choices can greatly alter image quality. Because ^{18}F PET has a more standardized imaging protocol (Franzius, Hotfilder et al. 2006; Hsu, Virk et al. 2008), this study will use that protocol to base both PET and SPECT acquisition parameters. In addition to acquisition parameters, it is also necessary to determine fixed imaging metrics in order to be able to unequivocally determine which modality is "better" for this application. The previous CT quantification study was performed using a tibia-injected model so that metastatic lesions would be formed in the same location across all animals. This study used a cardiac injection model of the same MDA-MB-231 cell line. Cardiac injection models allow metastases to form in multiple, unpredictable locations. Typically metastases will still form near the growth plate of

the hind limbs or forelimbs, but will also occasionally from on the ribs or spine. This variability allows for either a detection-based evaluation method or a quantification-based method.

Methods

Preliminary Radiation Dosimetry Determination

As previously discussed, radiation dose to bone in mice had already been determined for ^{18}F (Taschereau and Chatziioannou 2007), but dose estimations for ^{99m}Tc-MDP were needed. To obtain estimates of radiation dose to bone we worked with Dr. Mike Stabin (Department of Radiology, Vanderbilt University). In order to obtain dosimetry estimates, several different things had to be determined: an accurate physical representation of animal structure, photon and electron absorbed fractions at relevant energies, decay data associated with the specific tracer being used, and how long the tracer remained in different regions of the body. His group first used a realistic whole-body mouse phantom (MOBY) in a voxelized format in conjunction with the geometry and tracking particle transport toolkit (GEANT). Varying energy inputs and starting locations were simulated in order to determine tissue absorbed fractions (Keenan, Stabin et al. 2010). The specific absorbed fractions for organs in conjunction with tracer decay properties and tracer biodistribution allowed for an estimate of absorbed radiation dose to be determined. In order to estimate the final radiation dose, the biodistribution of ^{99m}Tc-MDP was needed.

Biodistribution data were collected from four mice using the Bioscan NanoSPECT system. Mice were retro-orbitally injected with between 1 to 1.5 mCi of ^{99m}Tc-MDP and were imaged at 0.5, 3, 7, 22, and 26 hours post injection using a 9-pinhole, high-sensitivity aperture (1.4 mm diameter) on each of the four camera heads. For 0.5, 3, and 7 hour time points images

were acquired with 60 seconds per projection and 24 projections for a total scan time of approximately 40 minutes, while images at 22 and 26 hour time points had 120 seconds per projection and 24 projections for a total scan time of approximately 90 minutes. SPECT images were reconstructed using an ordered subset expectation maximization (OSEM) algorithm, giving x and y dimensions of 124 × 124 voxels, with the z-dimension being determined by the length of the animal and its positioning on the bed such that the entire animal was in the field of view. Voxels were reconstructed to be 0.3 × 0.3 × 0.3 mm^3. All SPECT imaging was performed using a 20% energy window from 140 keV. Images were converted to activity units using a standardized procedure that uses a phantom-derived quantification factor. For each time point ROIs were drawn around the skeletal activity and over the entire image and then summed to determine the total activity present. This total activity was divided by the injected dose to give units of percent of injected dose. These values were plotted to form two different time activity curves for each mouse, one showing percent of injected dose over time of the whole body and the other only in the skeletal region. These time-activity curves were then individually used to estimate radiation dose and the four resulting sets of dosimetry numbers were averaged to determine a final estimate of absorbed dose per injected activity.

Preliminary Phantom Studies for Protocol Determination

In order for both PET and SPECT images to be comparable, images need to be acquired close enough in time to ensure that the metastatic state is the same. Ideally, this would encompass having both PET and SPECT imaged one after the other. But because both systems use similar mechanisms for detection of photons, there exists a potential for ^{18}F to distort the SPECT images and/or ^{99m}Tc to distort the PET images. Before a final protocol for this study is determined, this possible interaction and its effects must be investigated.

PET systems are designed to image 511 keV photons and use electronic collimation as opposed to physical collimation in order to determine the line of response of the incident photon. In addition, energy windows are applied to the acquired data to help discriminate between scattered and un-scattered photons. For all PET scans in this project, detected photons were subjected to an energy window of 350 keV to 650 keV, and all detected photons outside of this window were discarded. Also, the timing window used was 6 ns. The microPET Focus system has been previously characterized and was determined to have an energy resolution of 18.5% for the entire system (Tai, Ruangma et al. 2005). There is a potential of some of the 140 keV ^{99m}Tc photons to add noise to the system by altering the singles rates, but due to the energy windowing this is unlikely.

SPECT systems are generally designed to detect lower energy photons, with one of the higher-energy radioisotopes being ^{111}In (174 keV and 247 keV). The 9-pinhole collimator and the NaI scintillator are both designed to image photons in this range. The energy window used for all SPECT scans was ±20% of 140 keV. Manufacturer characterization reported that the Bioscan NanoSPECT system has an energy resolution of less than 9.7% on all four detectors. Although the 511 keV photons from ^{18}F fall outside of this accepted window, if any of these photons scatter and have a reduced energy it is possible that they could interact with the detector and cause additional noise in the system.

The potential effects of imaging both PET and SPECT on the same day were investigated through a series of phantom studies. First, a simple phantom was made that holds two syringes, as shown in Figure 15. Water-, ^{99m}Tc-, or ^{18}F-filled syringes in varying combinations were placed in the phantom and imaged in both the microPET Focus 220 and the Bioscan NanoSPECT Siemens systems. Three PET and three SPECT scans were acquired, each with the following syringe combinations: ^{18}F + H_2O, ^{99m}Tc + H_2O, and ^{99m}Tc + ^{18}F. PET scans were acquired with one

27

static frame for 5 minutes for each syringe combination and reconstructed to 128 × 128 × 95 voxels with sizes of 0.4745 × 0.4745 × 0.796 mm^3 using a 3D OSEM followed by an altered form of a maximum a posteriori (MAP) algorithm called fastMAP. Due to the large size of the phantom, SPECT scans were acquired with the 9-pinhole rat aperture (2.5mm diameter) with 24 projections and 60 seconds per projection for a total acquisition time of approximately 15 minutes. SPECT images were reconstructed to 114 × 114 × 110 voxels at 0.6 × 0.6 × 0.6mm^3 using an OSEM algorithm. At start of imaging, syringes held approximately 200μCi of ^{99m}Tc and ^{18}F and were filled to a volume of 1.5mL with saline. The control water syringe was also filled to 1.5mL. PET imaging was performed first with each combination, followed by SPECT imaging.
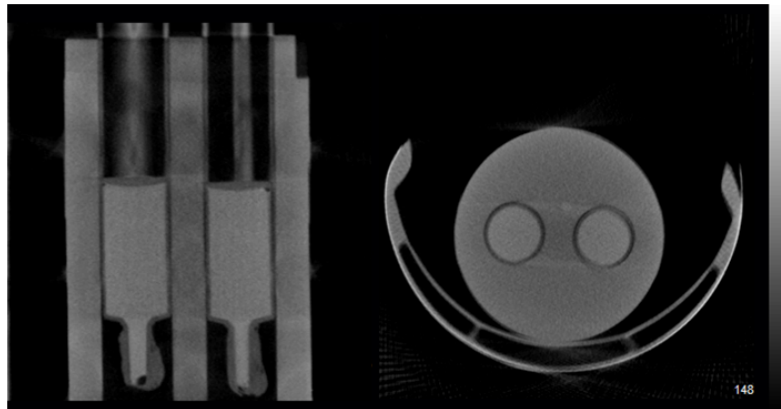
Figure 15: CT image of 2-syringe phantom, shown with two syringes present.

Following the initial investigation, further interrogation of the effects of ^{18}F in SPECT was performed in order to determine how different ratios of the tracers affected image quality. A series of scans over time was taken with just the ^{99m}Tc + ^{18}F syringe combination using the same phantom. Imaging the ^{99m}Tc + ^{18}F syringe combination over a period of time leads to a differing ratio of activities as ^{18}F decays much faster than ^{99m}Tc. At the first scan time, an ^{18}F and a ^{99m}Tc syringe with 212μCi and 440μCi, respectively were imaged using the same SPECT imaging

protocol as above. SPECT scans were then repeated approximately hourly for a total of 5 scans. This corresponded to imaging the following ratios of ^{99m}Tc to ^{18}F: 2.07, 2.66, 3.56, 4.60, and 6.18. SNR of the ^{99m}Tc-filled syringe to background at each ratio was determined.

Final PET SPECT Comparison Protocol

Nude mice were cardiac-injected with the metastatic breast cancer cell line MDA-MB-231. The resulting bone lesions were imaged with the Siemens microPET Focus 220 and the Bioscan NanoSPECT. Mice were imaged three weeks after cell injection to ensure tumors were of a reasonable size. Based on results from the preliminary phantom study, animals were imaged on the same day with SPECT imaging occurring before PET in order to eliminate the deleterious effects of ^{18}F in SPECT. Three mice were retro-orbitally injected with approximately 3.28mCi of ^{99m}Tc-MDP and were imaged with SPECT beginning 2.5 hours after injection. Before moving the mouse off of the SPECT bed, a low-dose CT was acquired with the CT system connected to the Bioscan NanoSPECT/CT system. This CT was only used for registration purposes. Following SPECT imaging, mice were retro-orbitally injected with approximately 250µCi of ^{18}F and PET images were acquired 1 hour post-injection. Mice were anesthetized with 2% Isofluorine during imaging and immediately prior to injection, but were awake during the 2.5 hour and 1 hour uptake times. Following PET acquisition, the bed holding the mouse was then moved into the Imtek MicroCAT for a low-dose CT that was also used for registration purposes. SPECT images were acquired with high-resolution 9-pinhole apertures (1.0 mm diameter) with 60 seconds per projection and 24 projections for a total scan time of approximately 35 minutes and reconstructed with an OSEM algorithm to have 124 × 124 × 313 voxels at 0.3 × 0.3 × 0.3mm^3. Because the entire field of view is necessary due to the uncertainty of tumors grow locations, SPECT acquisitions were set up to image the entire mouse. PET images were acquired

with one static, 30 minute frame using a continuous bed motion protocol to image the entire mouse. Reconstruction with the standard fastMAP algorithm is not possible when using a continuous bed motion protocol, so a 2D OSEM algorithm was used instead. Images were reconstructed to have 128 × 128 voxels with varying z-dimensions with a 0.4 × 0.4 × 0.796 mm^3. In order to create as similar scans as possible between PET and SPECT, both the duration of image acquisition and the axial field of view were made the same. Also, tracer uptake time was set to be approximately half of one half-life for both tracers, as a 1 hour uptake time for ^{18}F PET was commonly used while a range of 1 hr to 3 hrs was found in the literature for ^{99m}Tc-MDP SPECT.

The mice used in this final comparison study were cardiac-injected as opposed to using the tibia-injected method because the cardiac method allows for more natural, random occurrence of metastatic growth. It was thought that by using this model a detection-based comparison could be performed in addition to quantifying differences in uptake. In the three mice that were imaged the location of the tumors were consistently in the same location at the knee joint and due to their small size were visually indistinguishable in both ^{18}F PET and ^{99m}Tc MPD SPECT images. Tumor locations were determined using fluorescence imaging of GFP which is expressed in this cell line with the CRI Maestro. Several quantification methods were attempted in order to determine how well both modalities were able to image osteolytic metastases.

There is unpublished data obtained by Dr. Julie Sterling that suggests there is an increase in total skeletal tracer uptake in the presence of a metastatic lesion when compared to a healthy subject's uptake. This effect could skew quantification methods that use a healthy region of bone in the same animal as a control. Because of this, two tibia-injected mice were imaged using a similar protocol at a time point when lesion size was very small and can be

considered as a control. Images were acquired using the same SPECT and PET protocol as the 3

mice study, only the SPECT images were acquired with the standard 9-pinhole aperture (1.4mm

diameter) and the PET images were acquired without continuous bed motion. Because voxel

values represent either activity or activity concentration for SPECT or PET respectively, and

these changes do not affect voxel size, these slight protocol differences should have no effect on

quantification.

All images were first changed to be in intensity units of percent of injected dose per

gram (%ID/g). SPECT data is automatically reconstructed to have units of MBq, and was

converted to %ID/cc by dividing by the injected activity and the volume of the voxel. PET data

was converted to concentration units (nCi/cc) using an activity calibration factor, and

subsequently divided by ID to have final units of %ID/cc. Based on the assumption that tissue

has a density of 1 g/cc, these units are then converted to %ID/g. Next, bladders were cropped

out of the images as the varying amounts of activity in them can skew the image's maximum

intensity. ROIs were then drawn to encompass all of the detected activity around the region of

the tibia; Figure 16 shows representative ROIs for one mouse in both PET and SPECT images.

Finally, for quantitative analysis the maximum value, volume, sum and average intensity of each

ROIs were determined. Because ROIs were drawn generously around the knee joint in order to

guarantee that all activity was included, voxels were only included in the calculations if the

intensity of the voxel was greater than 0.25 times the average maximum intensity of the control

mice. This avoids underestimation of the mean ROI activity due to very low-signal voxels and

overestimation of the total ROI volume.
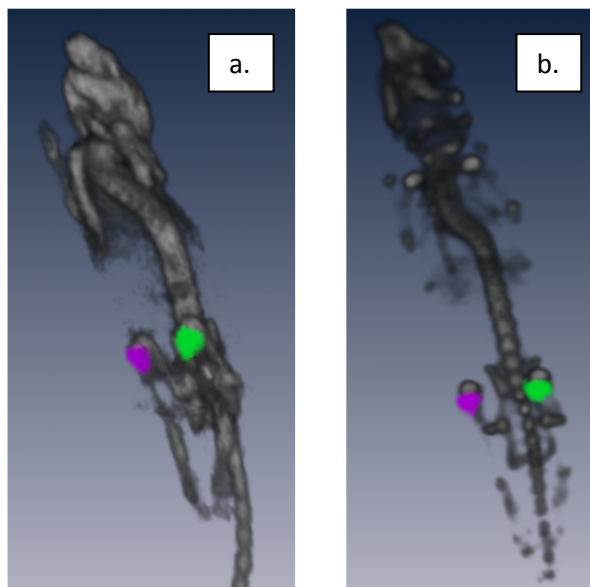
Figure 16: Shows representative ROIs for limb 1 and limb 2, purple and green, respectively for both (a) PET and (b) SPECT.

Results

Preliminary Radiation Dosimetry Determination

The time activity curves for skeletal and whole-body uptake of ^{99m}Tc-MDP for the four mice can be seen in Figure 17 and Figure 18. Skeletal uptake ranges from 14% to 18% of injected dose at the earliest time point and is mostly out of the system by around 24 hours. Whole-body uptake has a similar trend to that of skeletal uptake, except with a higher initial range. This higher range drops out quickly due to clearance of the tracer through the bladder. This data was used by Dr. Mike Stabin as input into his dosimetry model, which resulted in Table 4. Also, the results for ^{18}F are shown for comparison. As the cancer model used in this study develops in bone, the primary area of concern for radiation dose is the dose absorbed by the bone, or osteogenic cells. Because of this, we will use the average 4.8765 mGy/MBq of absorbed dose for ^{99m}Tc-MDP in conjunction with the already known value of 64 mGy/MBq for ^{18}F (Taschereau and Chatziioannou 2007). This result shows that one can inject approximately 1MBq of ^{18}F for every

32

10MBq of ^{99m}Tc-MDP to have equal radiation dose to the subject for each. A standard ^{18}F protocol with an injection of 9.25MBq (250μCi) of ^{18}F, injecting 121.36MBq (3.28mCi) of ^{99m}Tc-MDP would result in each tracer delivering an absorbed dose of 592mGy to the skeleton.
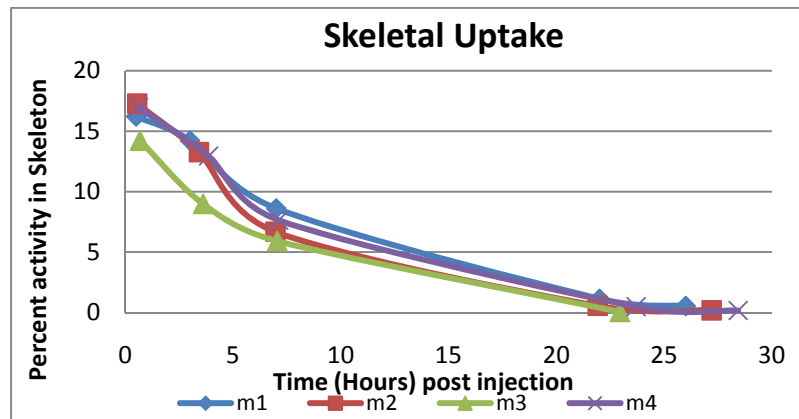
Figure 17: Time acitivty curves of skeletal uptake in four mice. Percent of injected activity decreases to almost zero in all mice by the 22 to 26 hour time point.
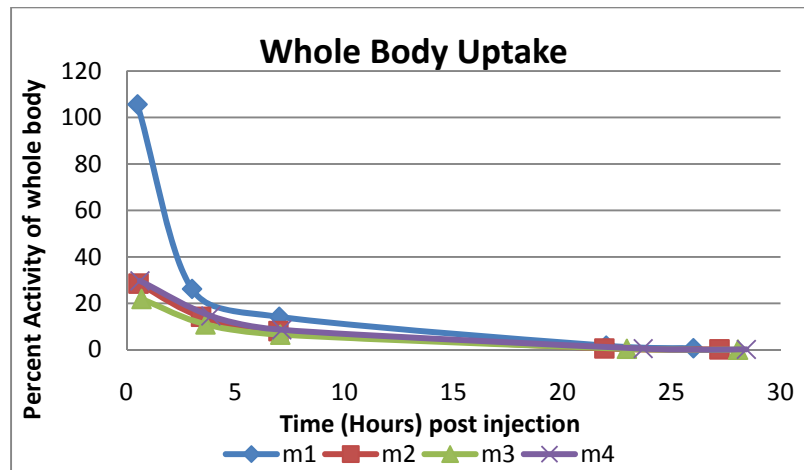
Figure 18: Time activity curve of whole body uptake in four mice with percent of injected activity decreasing over time.

Table 4: Shows average radiation dose per injected activity received to specific organs for both the published ^{18}F tracer (Taschereau and Chatziioannou 2007) and the ^{99m}Tc-MDP tracer determined by using the RADAR model.

|	^{99m}Tc-MDP Dose (mGy/MBq)				^{18}F Dose
	Average	Std Dev	Min	Max	mGy/MBq
Brain	0.4006	0.0985	0.3044	0.5376	13.0
LLI Wall	0.3679	0.1036	0.2708	0.5139	NA
Small Intestine	0.3297	0.1086	0.2269	0.4825	NA
Stomach Wall	0.3620	0.1151	0.2510	0.5229	4.0
Heart Wall	0.4555	0.1232	0.3357	0.6271	8.0
Kidneys	0.3422	0.1185	0.2285	0.5082	16.0
Liver	0.3948	0.1252	0.2738	0.5698	8.0
Lungs	0.8848	0.1612	0.7256	1.1074	11.0
Pancreas	0.3202	0.1164	0.2087	0.4834	8.0
Red Marrow	4.8765	0.5041	4.3620	5.5565	66.0
Osteogenic Cells	4.8765	0.5041	4.3620	5.5565	64.0
Spleen	0.2776	0.1000	0.1817	0.4178	7.0
Testes	0.3842	0.0649	0.3277	0.4771	9.0
Thyroid	0.5523	0.1251	0.4298	0.7260	5.0
Urinary Bladder Wall	30.9257	9.1365	18.9949	41.2496	333.0
Total Body	0.8307	0.0977	0.7389	0.9672	10.0

Preliminary Phantom Studies for Protocol Determination

Resulting images from the PET and SPECT syringe combinations of ^{18}F + H_2O, ^{99m}Tc + H_2O, and ^{99m}Tc + ^{18}F can be seen in Figure 19 and Figure 20, respectively. PET images with or without ^{99m}Tc showed very little difference in image quality. Image quality was quantified by calculating SNR, with the average value of an ROI of the activity in the syringe divided by the standard deviation of an ROI in the background. SNR was calculated for ^{18}F + H_2O and ^{99m}Tc + ^{18}F, and found to be 1009.7 and 965.5 respectively. The only major concern with imaging PET with ^{99m}Tc present is that there will be a higher random coincidence rate if there is an increase in the number of singles counts present. But, singles counts between these two scans only varied by 4.5%, while the raw singles rate was 43.38% higher with the ^{99m}Tc-filled syringe present.
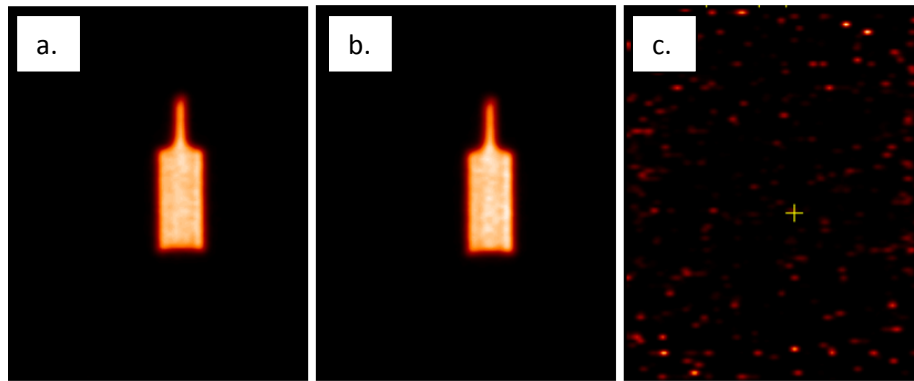
Figure 19: Panel a, b, and c show representative slices of PET scans of the ^{99m}Tc + ^{18}F, ^{18}F + H$_2$0 and ^{99m}Tc + H$_2$0 syringe combination respectively. Simple visual inspect shows little difference between the PET images with and without ^{99m}Tc present.
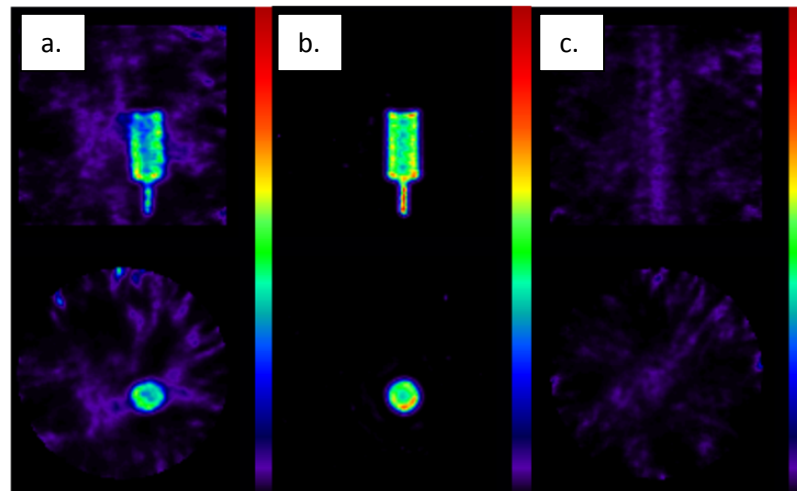
Figure 20: Panel a, b, and c show representitive slices of SPECT images of the ^{99m}Tc + ^{18}F, ^{99m}Tc + H$_2$0, and ^{18}F + H$_2$0 syringe combination respectively. Visual inspection shows the degradation in image quality when ^{18}F is present in the scans.

Unlike PET, SPECT images were greatly altered by the presence of ^{18}F. The SNR of syringe with ^{99m}Tc + H$_2$0 was found to be 334, while SNR of ^{99m}Tc + ^{18}F was only 25. This large difference is apparent in the images shown in Figure 20. After the determination of poor image quality, a series of images were acquired with the same phantom setup to determine how image quality of SPECT with ^{99m}Tc + ^{18}F changes at varying concentration ratios. Image SNR was determined

and the changes in image SNR can be seen in Figure 21. As expected the SNR increases as less ^{18}F activity is present.

SPECT SNR with ^{18}F and ^{99m}Tc
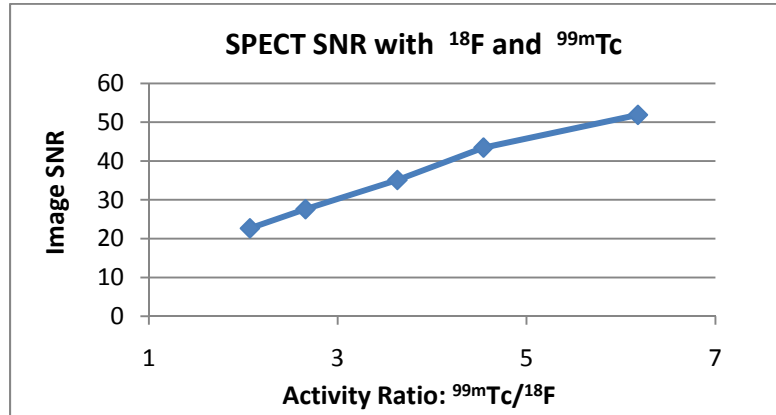
Figure 21: Graph shows increasing SNR due to increasing ratio of ^{99m}Tc to ^{18}F. Less ^{18}F present allows for better SPECT image quality.

Final PET SPECT Comparison Analysis

First, both PET and SPECT images were visually inspected for differences between lesion regions and healthy bone. By optical imaging of GFP, tumor cells were determined to be growing just below the knee joint in both hind limbs of mouse 1, and in one hind limb of both mouse 2 and mouse 3. Because of the increased uptake of both tracers at the ends of the long bones there was little visual evidence of a bone lesion in either PET or SPECT images. Representative PET and SPECT images can be seen in Figure 22. Unfortunately, in these subjects no lesions formed in areas such as the ribs or spine, which likely would have been easier to detect. Results for various quantification methods can be seen in Table 5. Limb 1 in all three mice has a small lesion, along with limb 2 in mouse 1.

36
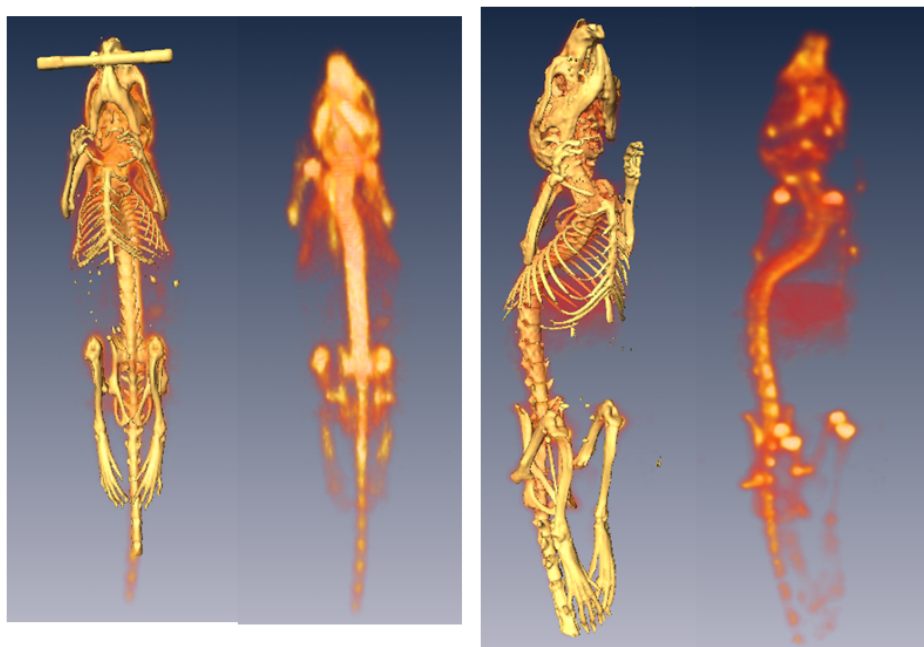
Figure 22: Representative volume rendering of cardiac-injected mouse. Left image set shows PET image with and without CT present, while right image set shows SPECT image with and without CT. Both knee regions have lesions present, but are not visible in the volume renderings.

Table 5: Shows ROI quantification of maximum image intensity, sum of image intensity, volume of ROI and average intensity in a, b, c, and d respectively.

a) ROI Max (%ID/g)		PET	SPECT
Mouse 1	Limb 1	20.41	48.28
	Limb 2	19.52	48.72
Mouse 2	Limb 1	32.28	43.35
	Limb 2	34.98	42.22
Mouse 3	Limb 1	33.97	66.64
	Limb 2	31.04	58.25

b) ROI Sum		PET	SPECT
Mouse 1	Limb 1	1969	6990
	Limb 2	1538	7393
Mouse 2	Limb 1	4922	5521
	Limb 2	2857	5611
Mouse 3	Limb 1	3879	9008
	Limb 2	4035	8714

c) ROI Volume (mm^3)		PET	SPECT
Mouse 1	Limb 1	24.84	8.15
	Limb 2	20.25	8.99
Mouse 2	Limb 1	45.09	6.86
	Limb 2	26.49	7.24
Mouse 3	Limb 1	35.66	9.50
	Limb 2	37.32	9.86

d) ROI Mean (%ID/g)		PET		SPECT	
		Mean	Std Dev	Mean	Std Dev
Mouse 1	Limb 1	10.10	3.36	23.15	9.37
	Limb 2	9.67	3.13	22.20	8.44
Mouse 2	Limb 1	13.90	7.08	21.74	8.15
	Limb 2	13.74	6.76	20.94	6.94
Mouse 3	Limb 1	13.85	6.47	25.59	12.45
	Limb 2	13.77	6.51	23.87	10.85

Comparing max, sum, volume, or average ROI intensities in mouse 2 and 3 would ideally result in differences between limb 1 and limb 2 due to the lack of lesion in limb 2 of those mice. But as can be seen from the tables, there is most likely not a significant difference between these values and in some cases they follow the opposite of the expected trend. For example, in the calculation of the volume of the ROI above the given threshold, in mouse 3's PET and SPECT data limb 2 has a higher volume than limb 1 even though it was expected that limb 1 would have more bone turnover and therefore a higher number of voxels in the volume count. In some cases PET has lower limb 1 than limb 2 values while SPECT has the expected trend (ROI max, mouse 2) while others show opposite trends (ROI Volume, mouse 2).

Discussion

Preliminary Radiation Dosimetry Determination

It was determined that the absorbed radiation dose to bone with ^{99m}Tc-MDP is only 4.88 mGy/MBq while from ^{18}F it is 64.0 mGy/MBq. Photons from ^{19}F have a high energy of 511 keV, making it much less likely to become scattered and absorbed in the animal than 140 keV photons from ^{99m}Tc. The majority of this difference is actually due to the energy deposited in the tissue from the positron that precedes gamma emission. Because ^{99m}Tc's decay mechanism does not involve positron emission, there is much less absorbed radiation dose in small animals. The injected tracer activity used in this study was determined by starting with a standard ^{18}F imaging protocol (Hsu, Virk et al. 2008) and choosing the amount of ^{99m}Tc-MDP to match the radiation dose of ^{18}F. SPECT is known to have a sensitivity in the range of 10^{-10} to 10^{-11} mol/L while PET's sensitivity is estimated to be higher, approximately 10^{-11} to 10^{-12} mol/L (Levin 2005). But when injecting more than 10 times the amount of activity compared to PET, this disadvantage is largely overcome.

Preliminary Phantom Studies for Protocol Determination

The ideal protocol for this study would involve imaging one modality directly after the other. But because both PET and SPECT image photons, there is a potential for unwanted interactions with the opposite tracer present. It was shown that having ^{99m}Tc present when imaging PET does not affect image quality. This is thought to occur because the lower ^{99m}Tc energy (140 keV) is detected, but falls outside of the energy window for inclusion in the coincidence event data. This explains why the raw singles count is extremely high compared to the actual singles count, as the raw count shows the total singles before application of the energy window, while the actual singles count only includes the ones in the acceptable energy-window. Because there is only a small difference in actual singles counts between PET imaging with and without ^{99m}Tc present there is likely little to no effect on the number of random coincidences detected as well.

On the other hand imaging SPECT with ^{18}F present has a detrimental effect on image quality. The collimators used with the NanoSPECT are not designed to efficiently stop photons at 511 keV. After photons pass through the collimators, they interact with the NaI detectors, which are also not designed to detect high energy photons. With the detector's lower stopping power, the 511 keV photons are more likely to Compton scatter in the detector, ejecting a secondary scattered particle and depositing a varying amount of energy into the detector. The absorbed energy on the detector has a very wide range, causing an overall increase in counts across the energy spectrum, including in the energy window used for ^{99m}Tc. This then leads to the added noise in the images.

Even with varying concentrations of tracer present, there is still an effect of ^{18}F in the SPECT images, and it was therefore decided to image SPECT ^{99m}Tc-MDP first and then inject ^{18}F

before performing the PET imaging. This protocol will eliminate any SPECT image degradation due to ^{18}F being present while still allowing for both PET and SPECT images to be acquired on the same day. Due to the uptake time of ^{18}F, PET images were acquired 1 hour after SPECT.

Final PET SPECT Comparison Analysis

Although tumors were not detectable in either PET or SPECT images, the quantification methods give some insight into each modality's ability to detect small changes in bone metabolism. Mixed results currently do not have the ability to determine which modality reliably allows determination of osteolytic bone lesions. These results could be different if the osteolytic lesions were larger at the time of imaging. Despite lack of ability to detect lesions or to have concrete quantitative proof as to which modality has better results with the present data, some additional considerations may help to better clarify results.

Examining the ability to visualize individual vertebrae in the spine may give insight into which modality can better detect bone lesions. From simple visual inspection of Figure 22, the spine appears to be better defined in the ^{99m}Tc-MDP SPECT image than the ^{18}F PET. This could be due to the combination of higher spatial resolution and higher injected activity. Another area to consider is the ability to detect the presence of the fibula. Although not incorporated into the drawn ROIs, sometimes small portions of the fibula could be seen. Figure 23 shows an example of PET and SPECT fibula uptake. It can be seen that SPECT imaging has a clearer region of where the tibia is present when compared to PET, where it is much more difficult to visually identify. Although visualization is important, it does not guarantee that ^{99m}Tc-MDP SPECT images will have better bone lesion to healthy bone contrast than ^{18}F PET due to the different ways in which they biologically interact with bone. Also, even though SPECT images have better spatial resolution it does not necessarily overcome its lower sensitivity limitations.
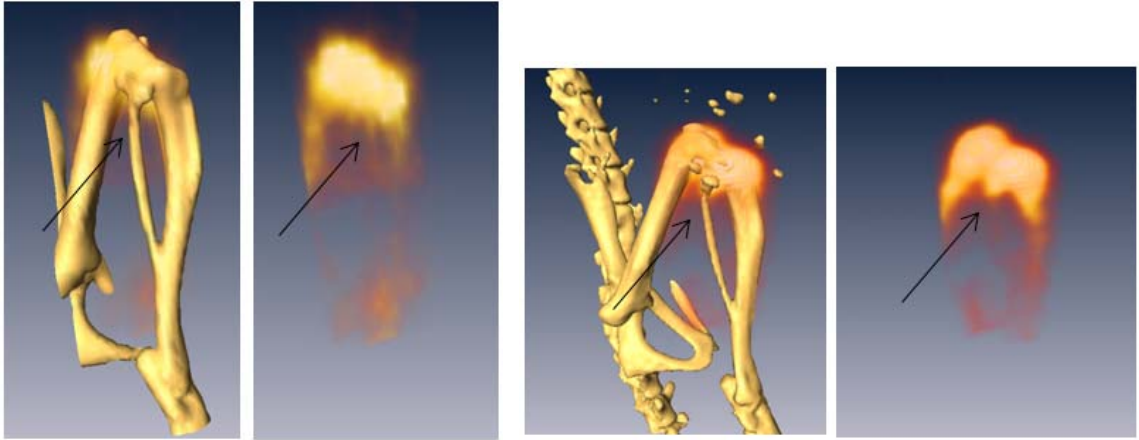
Figure 23: Panel a shows a close up view of PET image with and without CT and panel b shows SPECT images with and without CT. Arrows indicate region where fibula is present.

CHAPTER IV

CONCLUSIONS

CT Quantification of Tumor-Induced Bone Loss

This project shows that quantification of changes in tibia volumes over time is possible using high-resolution microCT images. Changes in group volumes between a treatment and non-treatment group were found to be statistically significant. This protocol has the potential to detect smaller changes in bone volumes at an earlier time point if it were to be used on a CT scanner with better performance. The quantification processes developed in this project can also be applied to other types of studies that involve monitoring changes in bone volume such as fracture healing or drug treatment effects on osteoporosis. Another area of interest this methodology could be applied to is imaging of osteoblastic tumors in bone. There are currently very few methods of quantifying how much bone volume is due to new, abnormal growth besides post-mortem histomorphometry. Adapting this protocol to an osteoblastic model would allow for longitudinal studies to be performed.

PET SPECT Comparison

A dosimetry-based protocol was determined for functional bone imaging in order to compare PET and SPECT. The osteolytic lesions imaged under the described protocol were not large enough to significantly influence either PET or SPECT images under visual inspection or with quantitative methods. Visual inspection of regions in the image where lesions are not present imply that ^{99m}Tc MDP SPECT could be better able to visualize smaller structures than ^{18}F PET. One main limitation of this method was that when PET was acquired, a continuous-bed

motion protocol was used, forcing the reconstruction algorithm to be 2D-OSEM instead of the standard fastMAP algorithm. Although the differences in accuracy of 2D-OSEM and fastMAP are debatable, the ability to visually identify larger lesions could be different depending on the reconstruction algorithm. This should be considered a limitation of PET in general due the limited axial field of view of the Focus 220.

There are several different ways this project could be expanded upon. First, imaging multiple animals with the same-day PET and SPECT protocol at varying time points after the tibia-injection of tumor cells could allow for bone lesions to be the right size to be detected by only PET or SPECT. This can also be done with the cardiac-injected model. In addition, the inclusion of more mice in the study would increase the chance of finding lesions in other areas such as the ribs and spine, which could help elucidate which modality can better detect them. Another option would be to use an osteoblastic model, which has been detected using ^{18}F PET previously. Quantification could potentially give more significant results in the tibia-injected model as approximately the same amount of tumor cells will be localized in the same area in each mouse. Finally, using other tracers for PET and SPECT that have similar targets could allow for additional comparisons of the modalities outside of functional bone imaging.

REFERENCES

Beir, V. (1990). National Research Council, Committee on the Biological Effects of Ionizing Radiation (BEIR V), Health Effects of Exposure to Low Levels of Ionizing Radiation, Washington, DC: National Academy Press.

Bhattacharjee, D. and A. Ito (2001) Deceleration of carcinogenic potential by adaptation with low dose gamma irradiation. *In Vivo*, **15**,(1): 87-92.

Boone, J. M., O. Velazquez and S. R. Cherry (2004) Small-animal X-ray dose from micro-CT. *Mol Imaging*, **3**,(3): 149-158.

Bridges, R. L., C. R. Wiley, J. C. Christian and A. P. Strohm (2007) An introduction to Na(18)F bone scintigraphy: basic principles, advanced imaging concepts, and case examples. *J Nucl Med Technol*, **35**,(2): 64-76; quiz 78-69.

Chen, Y. W., M. Y. Huang, J. S. Hsieh, M. F. Hou, S. H. Chou and C. L. Lin (2007) Discordant findings of skeletal metastasis between tc 99M MDP bone scans and F18 FDG PET/CT imaging for advanced breast and lung cancers--two case reports and literature review. *Kaohsiung J Med Sci*, **23**,(12): 639-646.

Cowey, S., A. A. Szafran, J. Kappes, K. R. Zinn, G. P. Siegal, R. A. Desmond, H. Kim, L. Evans and R. W. Hardy (2007) Breast cancer metastasis to bone: evaluation of bioluminescent imaging and microSPECT/CT for detecting bone metastasis in immunodeficient mice. *Clin Exp Metastasis*, **24**,(5): 389-401.

Datta, H. K., W. F. Ng, J. A. Walker, S. P. Tuck and S. S. Varanasi (2008) The cell biology of bone metabolism. *J Clin Pathol*, **61**,(5): 577-587.

Even-Sapir, E. (2005) Imaging of malignant bone involvement by morphologic, scintigraphic, and hybrid modalities. *J Nucl Med*, **46**,(8): 1356-1367.

Even-Sapir, E., U. Metser, E. Mishani, G. Lievshitz, H. Lerman and I. Leibovitch (2006) The detection of bone metastases in patients with high-risk prostate cancer: 99mTc-MDP Planar bone scintigraphy, single- and multi-field-of-view SPECT, 18F-fluoride PET, and 18F-fluoride PET/CT. *J Nucl Med*, **47**,(2): 287-297.

Franzius, C., M. Hotfilder, C. Poremba, S. Hermann, K. Schafers, H. E. Gabbert, H. Jurgens, O. Schober, M. Schafers and J. Vormoor (2006) Successful high-resolution animal positron emission tomography of human Ewing tumours and their metastases in a murine xenograft model. *Eur J Nucl Med Mol Imaging*, **33**,(12): 1432-1441.

Gambhir, S. S. (2002) Molecular imaging of cancer with positron emission tomography. *Nat Rev Cancer*, **2**,(9): 683-693.

Guise, T. A., W. M. Kozlow, A. Heras-Herzig, S. S. Padalecki, J. J. Yin and J. M. Chirgwin (2005) Molecular mechanisms of breast cancer metastases to bone. *Clin Breast Cancer*, **5 Suppl**,(2): S46-53.

Guise, T. A., K. S. Mohammad, G. Clines, E. G. Stebbins, D. H. Wong, L. S. Higgins, R. Vessella, E. Corey, S. Padalecki, L. Suva and J. M. Chirgwin (2006) Basic mechanisms responsible for osteolytic and osteoblastic bone metastases. *Clin Cancer Res*, **12**,(20 Pt 2): 6213s-6216s.

Hamaoka, T., J. E. Madewell, D. A. Podoloff, G. N. Hortobagyi and N. T. Ueno (2004) Bone imaging in metastatic breast cancer. *J Clin Oncol*, **22**,(14): 2942-2953.

Hsu, W. K., M. S. Virk, B. T. Feeley, D. B. Stout, A. F. Chatziioannou and J. R. Lieberman (2008) Characterization of osteolytic, osteoblastic, and mixed lesions in a prostate cancer mouse model using 18F-FDG and 18F-fluoride PET/CT. *J Nucl Med*, **49**,(3): 414-421.

Kanishi, D. (1993) 99mTc-MDP accumulation mechanisms in bone. *Oral Surg Oral Med Oral Pathol*, **75**,(2): 239-246.

Keenan, M. A., M. G. Stabin, W. P. Segars and M. J. Fernald (2010) RADAR Realistic Animal Model Series for Dose Assessment. *J Nucl Med*, **51**,(3): 471-476.

Levin, C. S. (2005) Primer on molecular imaging technology. *Eur J Nucl Med Mol Imaging*, **32 Suppl 2**: S325-345.

Polascik, T. J. (2009) Bisphosphonates in oncology: evidence for the prevention of skeletal events in patients with bone metastases. *Drug Des Devel Ther*, **3**: 27-40.

Schirrmeister, H. (2007) Detection of bone metastases in breast cancer by positron emission tomography. *Radiol Clin North Am*, **45**,(4): 669-676, vi.

Schirrmeister, H., A. Guhlmann, J. Kotzerke, C. Santjohanser, T. Kuhn, R. Kreienberg, P. Messer, K. Nussle, K. Elsner, G. Glatting, H. Trager, B. Neumaier, C. Diederichs and S. N. Reske (1999) Early detection and accurate description of extent of metastatic bone disease in breast cancer with fluoride ion and positron emission tomography. *J Clin Oncol*, **17**,(8): 2381-2389.

Society, A. C. (2008). <u>American Cancer Society. Cancer Facts & Figures</u>. Atlanta, American Cancer Society.

Tai, Y. C., A. Ruangma, D. Rowland, S. Siegel, D. F. Newport, P. L. Chow and R. Laforest (2005) Performance evaluation of the microPET focus: a third-generation microPET scanner dedicated to animal imaging. *J Nucl Med*, **46**,(3): 455-463.

Taschereau, R. and A. F. Chatziioannou (2007) Monte Carlo simulations of absorbed dose in a mouse phantom from 18-fluorine compounds. *Med Phys*, **34**,(3): 1026-1036.

Teitelbaum, S. L. (2000) Bone Resorption by Osteoclasts. *Science*, **289**,(5484): 1504-1508.

Toegel, S., O. Hoffmann, W. Wadsak, D. Ettlinger, L. K. Mien, K. Wiesner, J. Nguemo, H. Viernstein, K. Kletter, R. Dudczak and M. Mitterhauser (2006) Uptake of bone-seekers is solely associated with mineralisation! A study with 99mTc-MDP, 153Sm-EDTMP and 18F-fluoride on osteoblasts. *Eur J Nucl Med Mol Imaging*, **33**,(4): 491-494.

Waarsing, J. H., J. S. Day, J. C. van der Linden, A. G. Ederveen, C. Spanjers, N. De Clerck, A. Sasov, J. A. Verhaar and H. Weinans (2004) Detecting and tracking local changes in the tibiae of individual rats: a novel method to analyse longitudinal in vivo micro-CT data. *Bone*, **34**,(1): 163-169.